



HAL
open science

Forming three-dimensional micro-objects using two-dimensional gradient printing

Aofei Mao, Peixun Fan, Loic Constantin, Nan Li, Xi Huang, Bai Cui,
Jean-François Silvain, Xinwei Wang, Yong Feng Lu

► **To cite this version:**

Aofei Mao, Peixun Fan, Loic Constantin, Nan Li, Xi Huang, et al.. Forming three-dimensional micro-objects using two-dimensional gradient printing. Applied Materials Today, 2022, 28, pp.101538. 10.1016/j.apmt.2022.101538 . hal-03693134

HAL Id: hal-03693134

<https://hal.science/hal-03693134>

Submitted on 10 Jun 2022

HAL is a multi-disciplinary open access archive for the deposit and dissemination of scientific research documents, whether they are published or not. The documents may come from teaching and research institutions in France or abroad, or from public or private research centers.

L'archive ouverte pluridisciplinaire **HAL**, est destinée au dépôt et à la diffusion de documents scientifiques de niveau recherche, publiés ou non, émanant des établissements d'enseignement et de recherche français ou étrangers, des laboratoires publics ou privés.

Forming three-dimensional micro-objects using two-dimensional gradient printing

Aofei Mao^{1,#}, Peixun Fan^{1,#,*}, Loic Constantin¹, Nan Li¹, Xi Huang¹, Bai Cui², Jean-Francois Silvain³, Xinwei Wang⁴, Yong Feng Lu^{1,*}

¹Department of Electrical and Computer Engineering, University of Nebraska, Lincoln, NE 68588, USA.

²Department of Mechanical and Materials Engineering, University of Nebraska, Lincoln, NE 68588, USA.

³CNRS, University of Bordeaux, Bordeaux I.N.P., ICMCB, UMR 5026, F-33608 Pessac, France.

⁴Department of Mechanical Engineering, Iowa State University, Ames, IA 50011, USA.

[#]These authors contributed equally to this work

^{*}Corresponding authors.

E-mails: ylu2@unl.edu. (Yong Feng Lu); fanpeixun@gmail.com. (Peixun Fan)

Abstract: Controllable transformations from two-dimensional (2D) patterns to three-dimensional (3D) geometries independent of materials or external stimuli are being pursued in numerous fields. Here, we present an approach to forming various 3D structures through 2D printing using distributed stress inside a polymer. The key is to establish controlled stress fields by introducing composition and property gradients inside a photocurable polymer by femtosecond laser two-photon polymerization. Structural deformation induced by internal stress is a general bottleneck both in materials processing and 3D printing. In contrast to the significant efforts previously made to reduce stress and deformation, we use them to enable shape transformation to construct various 3D micro-objects through 2D printing with engineered stress fields inside. Multi-mode 2D-to-3D structural transformations, including bending, rolling, coiling, waving, spiraling, and out-of-plane distortions are realized in a shape- and location-specific fashion. This strategy promises a unique way to fabricate delicate 3D objects not feasible through conventional techniques and to circumvent the intrinsic stepping limitations in direct 3D printing using two-photon polymerization. When combined with the standard 2D patterning techniques such as nanoimprint and photolithography, such a 2D-to-3D transformation approach will lay a foundation for high-throughput and cost-effective production of complex 3D nanostructures.

Keywords: controllable 2D-3D transformation, self-shaping, two-photon polymerization, femtosecond laser micro/nano manufacturing, anisotropic shrinkage, stress control

TPP	two-photon polymerization
fs	femtosecond
2D	two dimensional
3D	three dimensional
2D-3D	2D-to-3D
LP	laser power
SS	scan speed
HD	hatching distance
SD	slicing distance
DoC	degree of conversion

1 SEM scanning electron microscope

2

3

4 **Introduction**

5 Controllable structural transformation from two-dimensional (2D) patterns to three-dimensional
6 (3D) geometries is being pursued in various fields including microelectromechanical systems
7 [1,2], soft actuators [3], biomimics [4], and biomedical devices [5-7]. One traditional strategy is
8 to utilize bi-/multi-layer structures composed of different materials, and the mismatches of their
9 properties, such as thermal coefficient and solubility parameter [8,9]. Structural transformation
10 has also been realized using the unique responses of specific materials (e.g., hydrogels [10],
11 shape memory polymers [11], *etc.*) to external stimuli (e.g., light [12], temperature [13],
12 chemicals [14], magnetic [15], *etc.*). Origami and kirigami methods have also been developed for
13 structural transformation through the exquisite design of hinges and foldings [16], making use of
14 surface tensions [17,18], cell traction [19], bucklings [20], *etc.*, as the driving forces. However,
15 general approaches capable of realizing controlled 2D-to-3D (2D-3D) transformation to
16 construct 3D geometries with a single material in a single process have yet to be explored.

17 Direct laser writing via two-photon polymerization (TPP) has been known for maskless and
18 programmable 3D printing at meso-micro-nano scales. However, TPP has primarily been used to
19 directly print 3D designs with little control over the material properties and the subsequent
20 structural transformation. Recent studies reported the reconfiguration and motion of 3D
21 structures after printing by adding stimuli-sensitive compositions (e.g., hydrogels [21], graphene
22 [22], carboxylic groups [23], gold nanorod [24], and bovine serum albumin [25], *etc.*) into the
23 polymer resins. Spontaneous structural transformation from in-plane 2D patterns to out-of-plan
24 3D objects independent of specific material compositions can inspire broad interests in
25 micro/nanofabrication but has seldom been achieved.

26 Here, we use TPP to tailor the local cross-link gradients inside photocurable polymers with
27 submicron resolutions and, thus, to establish spatially distributed stresses for achieving
28 spontaneous, prespecified 2D-3D transformations (**Video S1**). Internal stresses usually cause
29 undesired structural deformations and, hence, are considered as a common bottleneck both in
30 materials processing and 3D printing. In contrast to the significant efforts previously made to
31 reduce stresses and deformations, we demonstrated that internal stresses can be tailored to form
32 3D micro-objects instead of directly printing geometries exactly as designed. The printing-
33 condition-determined degree of conversions (DoC) and shrinkage behaviors of polymers were
34 investigated. This research clarifies the critical role of composition and property gradients inside
35 a single material in enabling 2D-3D transformations. Multi-mode transformations were achieved
36 either individually in different shapes or simultaneously in a single complex 3D structure in
37 different photocurable polymers, revealing the universality of the 2D-3D transformation
38 approach. This strategy opens up a new avenue to fabricate 3D micro-objects with complex
39 geometries, reduces the production time cost, and circumvents the intrinsic stepping limitations
40 in direct 3D printing. The fundamentals explored in this study promise new opportunities for
41 addressing general challenges in the fabrication of 3D micro/nanoscale structures for different
42 applications.

43

44

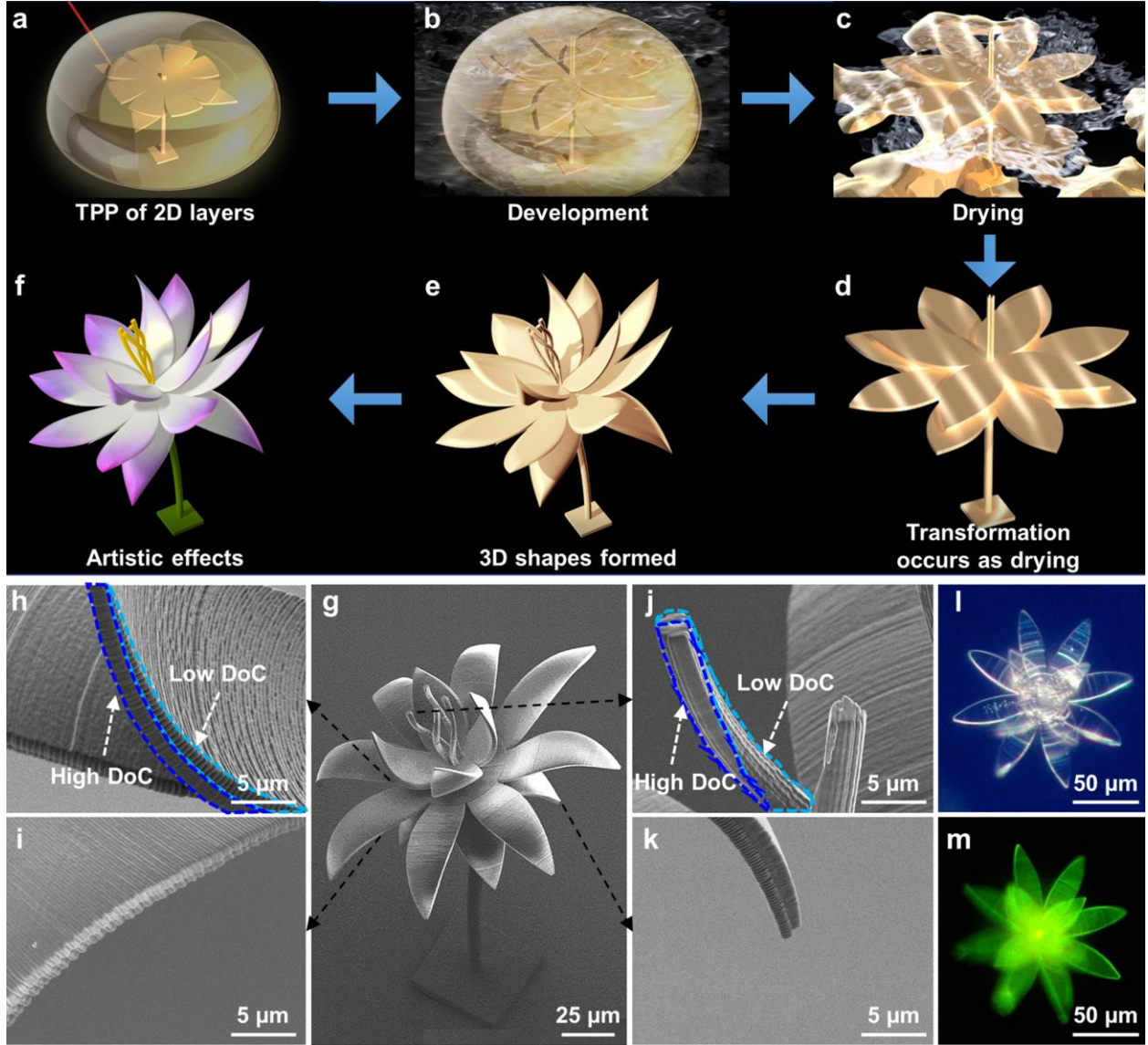
1 Results and discussion

2 *Conception of TPP-enabled 2D-3D transformation*

3 **Figure 1a-f** illustrate the processes involved in the TPP-enabled 2D-3D transformation approach.
4 The 2D in-plane patterns unfolded from targeted 3D objects are printed via TPP. In TPP, photo-
5 initiators absorb two photons simultaneously in response to femtosecond (fs) laser exposures and
6 decompose into free radicals. The sp^2 carbons from monomers react with surrounding free
7 radicals to form polymer networks until termination occurs. Subsequently, the unreacted
8 initiators and monomers are replaced and removed by developing agents. As the developing
9 agents dry up, the polymer networks tend to shrink [26]. The key step in the TPP-enabled 2D-3D
10 transformation approach is to introduce internal gradients in polymerization. Correspondingly,
11 the level of shrinkage will be location-specific in the 2D patterns, building up stress fields when
12 drying up and enabling the transformation of the 2D patterns to desired 3D objects [27].

13 As a nonlinear two-photon process, TPP occurs within a nanoscale ellipsoid around the fs
14 laser focal spot (voxel). This enables flexible and accurate control over the stress fields.
15 Specifically, the DoC from monomers to polymer networks directly determines the cross-link
16 densities and, thus, the shrinkage at different locations [28,29]. Since the DoC is laser-dose
17 dependent, the shrinkages and the consequent stress fields can be tailored voxel-by-voxel
18 through tuning the TPP printing parameters, including the hatching distance (HD), slicing
19 distance (SD), scan speed (SS), and laser power (LP). Therefore, the structural transformation
20 from in-plane 2D patterns to out-of-plan 3D objects can be controlled. More details of the 2D-3D
21 transformation approach and its mechanisms are shown in **Figs. S1-S3**.

22 As an example, **Fig. 1g** shows a 3D standing flower structure composed of a pedicle,
23 multiple petals at three different height positions and several stamens, which was fabricated
24 through the 2D-3D transformation. Different DoC gradients were introduced at different
25 locations during TPP printing. Specifically, the pedicle was printed such that one side was
26 polymerized to a higher degree than the other side. For the stamens, higher and lower DoC
27 regions varied spirally during the printing. In the petals, the DoC gradients were set along both
28 the thickness and the radial directions to achieve different curvatures. We succeeded in
29 simultaneously realizing different types of spontaneous 2D-3D transformations in the pedicle,
30 stamens and petals while keeping the entire flower free-standing. The stamens twisted to show
31 different helical shapes (**Fig. 1j**). Meanwhile, some petals bent upwards while others bent
32 downwards (**Fig. 1h, I, k**). The head of the pedicle bent towards the lower left together with the
33 stamens and petals, which can be more clearly seen from the zoomed images in **Fig. S4b**. The
34 dark-field and fluorescence images demonstrate that the 3D flower is intact and undamaged
35 during the transformation (**Fig. 1l, m**). Besides, **Fig. S4a** shows that an array of the 3D standing
36 flower were identically fabricated in one batch, confirming the reproducibility of the 2D-3D
37 transformation.



1
2 **Figure 1.** Overview of the spontaneous 2D-3D structural transformation. a-f) Schematics of the processes of the
3 2D-3D transformation approach. g) An overall SEM image of a standing flower after the 2D-3D
4 transformation. h-k) Zoomed-in SEMs of the stamens (j) and petals at three different heights (h, i, k). l) Dark-
5 field optical microscopy, and m), green-fluorescence images of the standing flower after transformation.
6

7 *Engineering stress field for directional 2D-3D transformation*

8 By printing individual cubic blocks with different TPP parameters, the “laser dose-DoC-
9 shrinkage” relationships were systematically analyzed. The DoC can be determined by
10 measuring the ratio of the C=C to C=O bonds before and after TPP using Raman spectroscopy
11 [30]. The volume shrinkage (S_v) was estimated by measuring the volume difference between the
12 printed and designed cubes and calculated as:

$$13 \quad S_v = \frac{V_0 - V}{V_0}, \quad (1)$$

14 where V_0 is the cube volume designed (i.e., $50 \times 50 \times 50 \mu\text{m}^3$ here), and V is the cube volume
15 measured after development. When the HD and SD are fixed, a higher laser dose (e.g., a higher

1 LP or a lower SS) results in a lower shrinkage and a higher DoC (**Figs. S5-S7**). Therefore, a
 2 negative correlation between the shrinkage and DoC is revealed, no matter either the LP or SS
 3 was used as the controlling factor (**Fig. 2a-b**). Besides, larger HDs result in higher shrinkages
 4 even that similar DoCs are reached, which becomes more obvious at lower DoC regions.

5 It was reported that the DoC of the IP-Dip resin (used in this research) can be correlated to
 6 the TPP parameters as [31]:

$$7 \quad DoC = c_1 \rho_0 \left(1 - e^{-\delta_{2,eff} c_0 \frac{LP^2}{SS} D_v} \right) + c_2, \quad (2)$$

8 where $c_1 \rho_0 = 0.62$, $c_2 = -0.15$, $\delta_{2,eff} = 3 \times 10^{-55} \text{ cm}^4 \text{ s}$, c_0 is a constant representing the relevant
 9 optical parameters used in TPP, and $D_v = c_3 / \text{HD}^n$ with $c_3 = 1.5e^4 \mu\text{m}^{-2.36}$ and $n = 0.64$. Using the
 10 TPP parameters—DoC and DoC—shrinkage correlations as a parameter-window indicator, the
 11 shrinkage of TPP samples can be controlled via controlling DoCs under different TPP printing
 12 conditions. Further, the shrinkage differences among different portions of the TPP samples can
 13 be designed and used to establish programmed stress fields. Through this effort, the stress fields
 14 can be utilized to control 2D-3D transformation rather than a detrimental factor that usually
 15 causes undesired deformations in TPP.

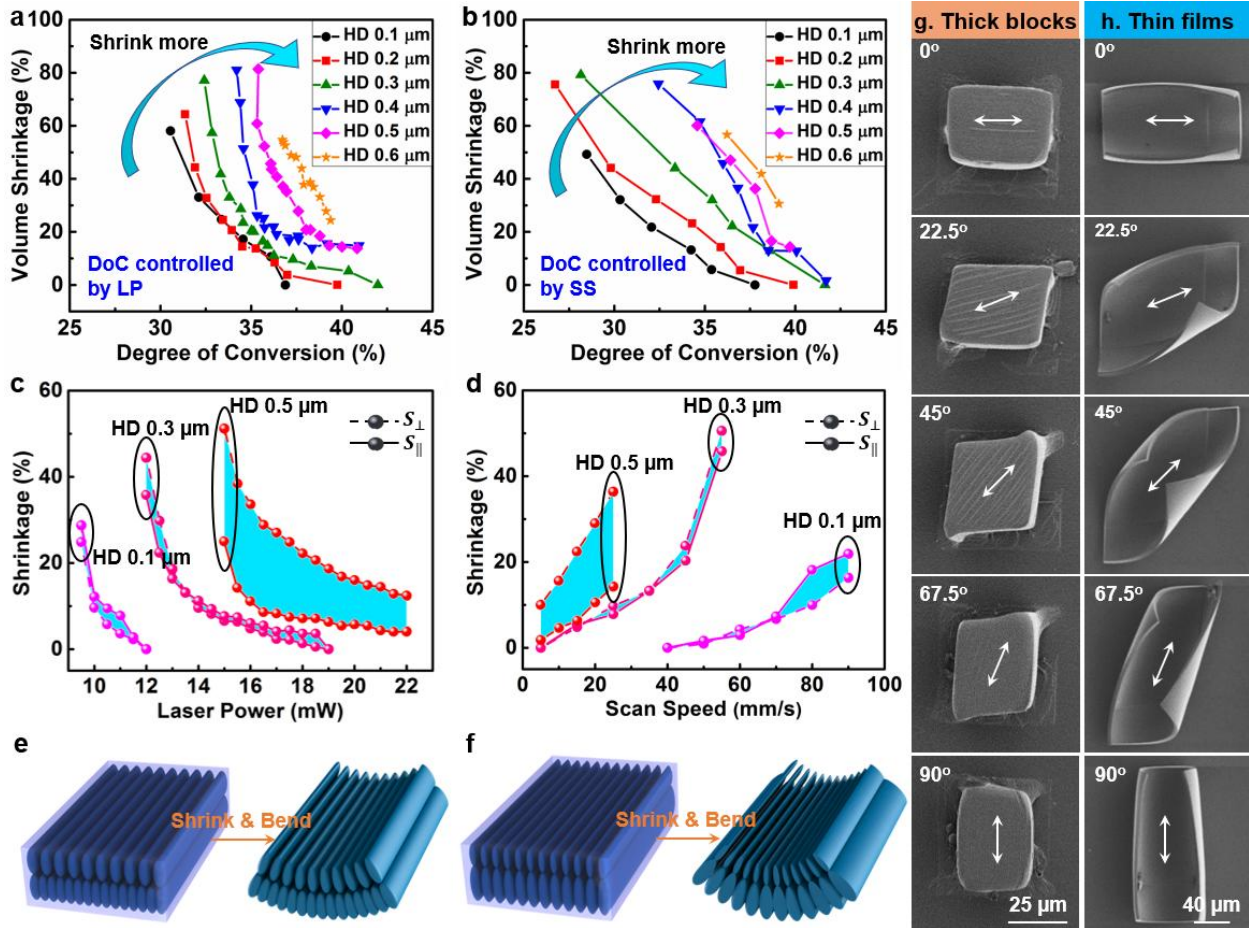
16 For 2D-3D structural transformation, anisotropic shrinkages are favored to gain directional
 17 control, which is essential for producing complex 3D structures from 2D patterns [16, 32-34].
 18 Our experimental results show that the HD plays a key role in the shrinkage anisotropy (**Figs. 2c-**
 19 **d, S8 and S9**). When small HDs (e.g., 0.1-0.3 μm) are used, the shrinkages are similar in both
 20 crossing directions, i.e., parallel (S_{\parallel}) and perpendicular (S_{\perp}) to the hatching direction. In contrast,
 21 using a large HD (e.g., $\geq 0.4 \mu\text{m}$) results in obviously higher shrinkages in the direction
 22 perpendicular to the hatching lines. Moreover, the shrinkage anisotropy can be tuned by the TPP
 23 parameters, e.g., LP and SS. When the HD is above 0.3 μm , the shrinkage anisotropy becomes
 24 more obvious with lower laser doses (e.g., lower LP or higher SS).

25 The anisotropic shrinkage originates from the Gaussian profile of the fs laser used, which
 26 results in DoC gradients along the radial direction in the cross-section of each polymer line (**Fig.**
 27 **S10**). During the overlap of TPP lines to cover a volume, the DoCs in the overlap regions
 28 between adjacent lines significantly determine the shrinkage behaviors. Using large HDs, lower
 29 DoCs are generated in the overlap regions than in the center of each line, making the overlap
 30 regions shrink more (**Fig. 2e**). Using lower LP or higher SS, polymer lines with smaller cross-
 31 sections are printed, which also causes lower DoCs in the overlap regions (**Fig. 2f**). Both
 32 conditions can make the whole printed volume inhomogeneous, with more shrinkage in the
 33 direction perpendicular to the TPP lines. When multiple layers are printed with different HDs,
 34 LPs or SSs, directional stress fields with controlled magnitudes can be established to enable 2D-
 35 3D transformation.

36 As a quantitative demonstration, **Fig. 2g** shows the SEMs of blocks ($50 \times 50 \times 50 \mu\text{m}^3$) printed
 37 with all the parameters fixed (LP = 19.5 Mw, SS = 10 mm/s, HD = 0.6 μm , and SD / HD = 2)
 38 other than the hatching direction rotated from horizontal (0°) to vertical (90°). The shrinkages are
 39 anisotropic and depend on the hatch direction. Further, taking the bending transformation as an
 40 example, the anisotropic shrinkage in thin films ($160 \times 160 \times 6 \mu\text{m}^3$) with DoC gradients
 41 intentionally introduced along the thickness direction was investigated (three layers were printed
 42 by setting HD/SD at 0.4/0.8, 0.3/0.6, and 0.15/0.3 μm , respectively, in the top, middle, and
 43 bottom layers). Theoretically, if the low DoC layers shrink isotropically, the thin films would

1 bend spherically because the second-moment inertia along both directions parallel and
 2 perpendicular to the hatching direction are equal due to identical geometries. However, the films
 3 rolled up with their axes parallel to the hatching directions (**Fig. 2h**), which indicates that the
 4 shrinkages of the low-DoC layers mainly occur in the direction perpendicular to the hatching
 5 direction. **Figure 2h** also verifies that the bending direction of the polymer films can be precisely
 6 and continuously tuned by simply changing the hatching direction. Therefore, the hatching
 7 direction can be used to control the path of the 2D-3D structural transformation provided that
 8 large HDs introduce sufficient DoC gradients (**Fig. S11**).

9 In addition to the bending directions, bending curvatures can also be controlled by tuning the
 10 anisotropy in shrinkage and the shrinkage difference between the adjacent TPP layers. To gain a
 11 deeper understanding of the 2D-3D transformation, we developed a simplified model to evaluate
 12 the bending trend of the TPP 2D films, where the 2D patterns can be equivalent to a series of
 13 local pairs of high- and low-DoC layers (**Fig. S12a-b**). It appears that the DoC differences in two
 14 adjacent layers determine the bending curvatures of the TPP films with the same thickness.
 15 Larger DoC differences result in sharper bending (**Fig. S12c-g**). The bending-DoC relation can
 16 guide the design of local bending to eventually control the overall 2D-3D transformations.



17
 18 **Figure 2.** Controlled anisotropic shrinkage through programmed DoC and directional 2D-3D transformation. a,
 19 b) Relationships between volume shrinkages and DoC with LP (a) and SS (b) as the controlling factors. c, d)
 20 Evolution of shrinkages with LP (c) and SS (d) at different HDs in both crossing directions. e, f) Schematics of
 21 anisotropic shrinkage and the consequent bending transformation perpendicular to the voxel lines through

1 controlling the line distance l and line width (f , g , h) Controlled anisotropic shrinkage of thick blocks (g) and
2 controlled bending of thin films (h) by tuning the hatching directions.

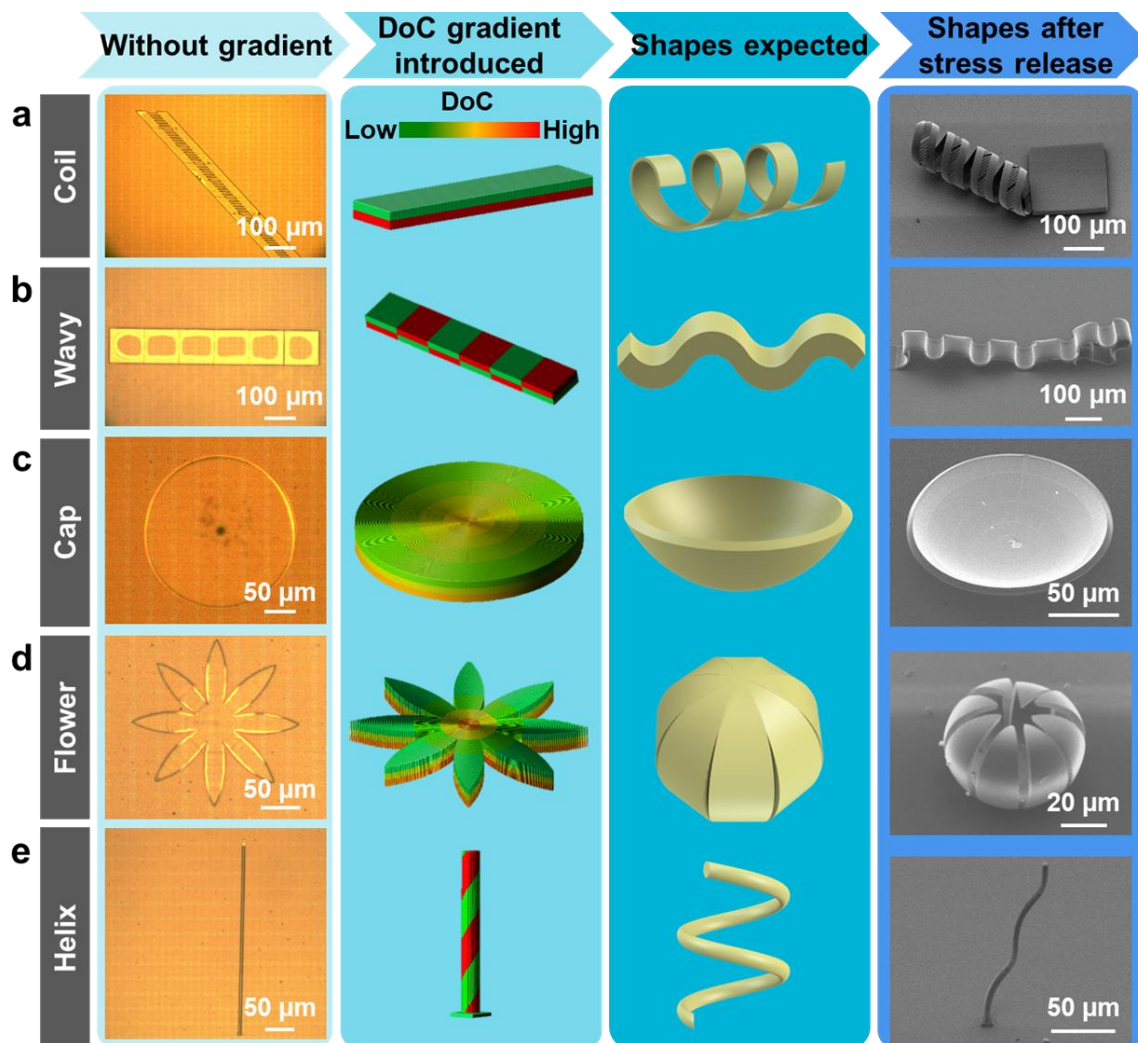
4 *2D-3D transformations to form diverse 3D structures*

5 With the programmable anisotropic shrinkage and stress fields, we can flexibly engineer the
6 polymer shrinkage by TPP and achieve diverse 3D structures transformed from 2D patterns. In
7 addition to the basic single-direction bending (namely rolling) in **Fig. 2h**, we have also realized
8 coiling transformation by generating DoC gradients in a 2D parallelogram pattern, forming a
9 microcoil with an even pitch and diameter (**Fig. 3a**). The hatching lines were made parallel to the
10 short edges of the parallelogram and the HDs increased from 0.2 μm at the bottom to 0.6 μm at
11 the top. In contrast, the same 2D pattern without DoC gradients remained flat after drying. The
12 advantages of free design in TPP can be applied to fabricate most complex structures. For
13 instance, by alternately reversing the DoC gradients at different lateral positions in a 2D pattern,
14 waving transformation was realized, producing a bi-curvature structure, such as a wavy strip (**Fig.**
15 **3b**).

16 Since the shrinkage is primarily determined by DoC, the DoC gradients can also be used to
17 generate out-of-plane distortions and even freeform transformations, leading to 3D structures
18 with dual-curvatures and ultimately spherical geometries. This is beyond what can be achieved
19 by simply bending and folding polymer films using conventional 2D-3D transformation routines
20 [35,36]. For example, we set the laser scan paths to concentric rings when printing a 2D circular
21 pattern and created DoC gradients along both the thickness and radial directions by changing the
22 HD and SD (**Fig. 3c**). After drying, the flat pattern was spontaneously transformed into a cap
23 shape. In comparison, the 2D circular pattern remained flat when no gradients were introduced.

24 To further demonstrate the capability of the 2D-3D transformation, microflowers were also
25 achieved by introducing DoC gradients along both the thickness and radial directions (**Fig. 3d**).
26 As a more general demonstration, we printed a microfiber with a diameter of 6 μm and a height
27 of 200 μm with the DoCs designed to have a spiral-like distribution (**Fig. 3e**). The straight fiber
28 was transformed to a helical shape after drying. We further explored the possibility of integrating
29 different types of transformations in a single complex structure and succeeded in producing an
30 entire standing flower (**Fig. 1g**), verifying the flexibility of the 2D-3D transformation to fabricate
31 objects with structurally complex components.

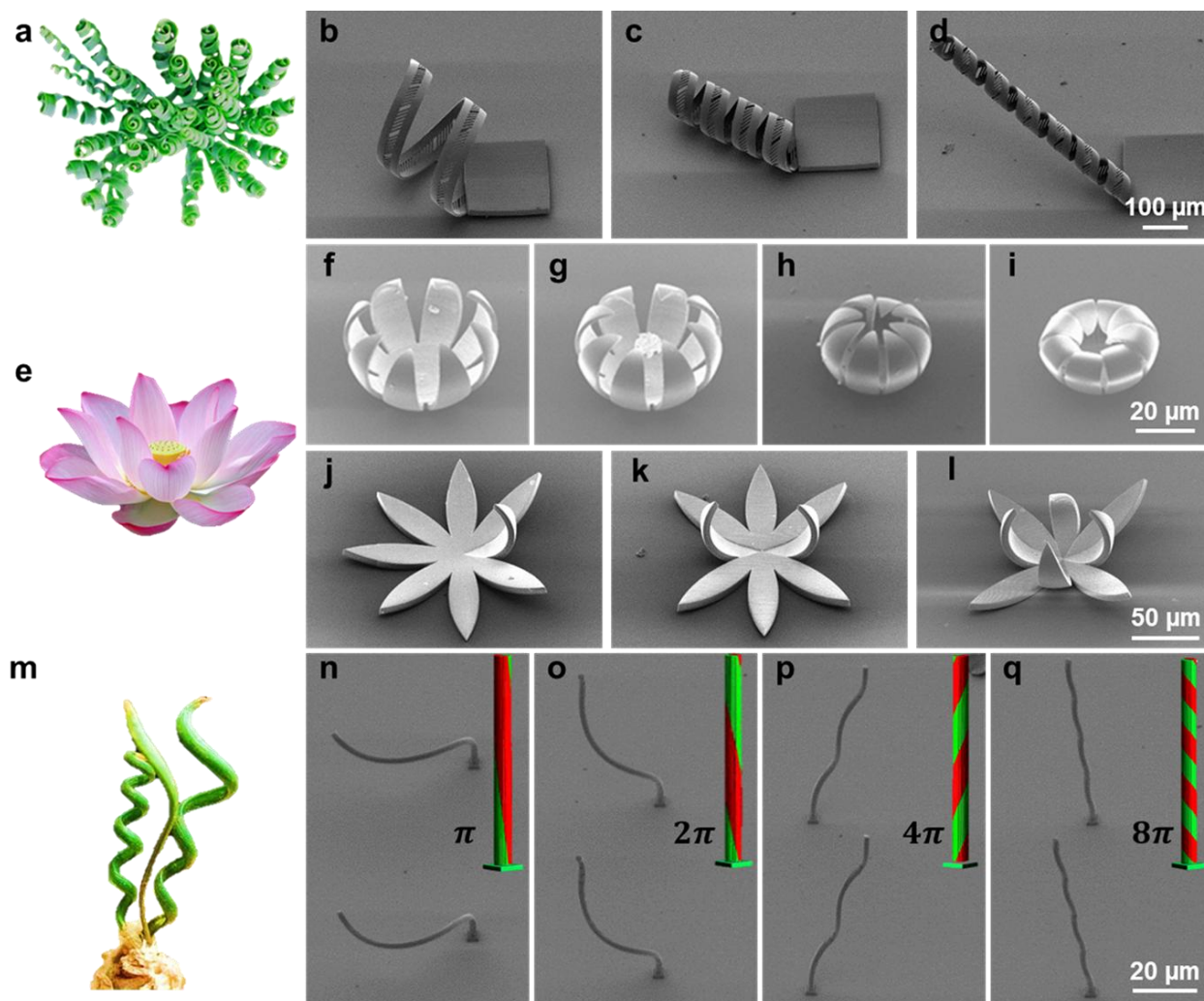
32 Besides, by adding specific features on the TPP 2D films, 3D micro-objects having
33 applications in different fields can be fabricated via the 2D-3D transformation. For example, we
34 have achieved a closed 3D microstent transformed from a 2D grid pattern by precisely tuning the
35 DoC gradients along the thickness direction, and a 3D micro-origami structure from a 2D three-
36 pointed-star plate by creating DoC gradients in the hinge regions (**Fig. S13**). The 3D microstent
37 and micro-origami structures have potential applications in biomedicine and
38 microelectromechanics, respectively. Additionally, a 3D curved truss structure was formed
39 through the transformation of a 2D flat pattern composed of multiple hexagon cells (**Fig. S14**).
40 The spaces within and among the cells provide more tunability on the 2D-3D structural
41 transformation.



1
2 **Figure 3.** Diverse structures achieved through multi-mode 2D-3D transformations. a) A coil structure formed
3 by creating DoC gradients along the thickness direction. b) A wavy structure formed by creating periodic DoC
4 gradients along the lateral direction. c, d) A cap I and a flower structure (d) formed by creating DoC gradients
5 along both the radial and thickness directions. e) A helical structure formed by manipulating DoC gradients.

6
7 *Shape- and location-specific 2D-3D transformation*

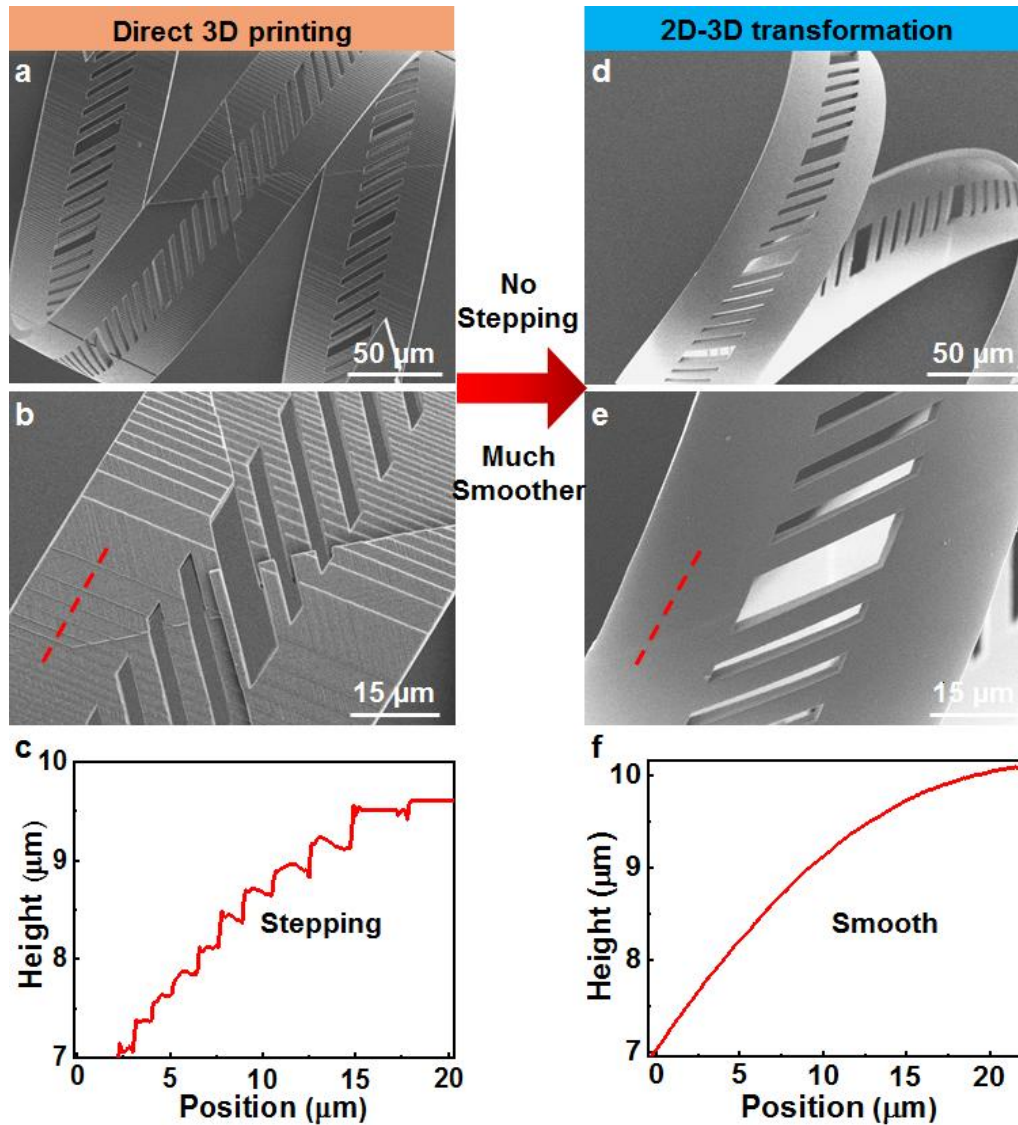
8 Furthermore, the 2D-3D transformation is quantitatively controllable, making shape- and location-
9 specific transformations possible. The shape- and location- specific transformation can be used
10 to mimic unique morphologies and different growing stages of natural plants. For example,
11 microcoils with two to six turns and diameters of 60-240 μm were formed from 2D patterns of
12 the same size (**Fig. 4b-d**), mimicking the curls of the *albuca namaquensis* grass (**Fig. 4a**).
13 Different bending effects were also realized through gradually increasing the DoC gradients
14 along the radial direction (**Fig. 4f-i**), mimicking the lotus flowers in different blooming stages
15 (**Fig. 4e**). The 2D-3D transformation can also tailor a specific one or more petals of the flower
16 structure (**Fig. 4j-l**) and occur to different degrees at each of the eight petals (**Fig. S15**).
17 Moreover, microhelices with different spins were fabricated by manipulating the DoC gradients
18 in periodicities of π , 2π , 4π , and 8π at a fixed height (**Fig. 4n-q**), mimicking the spiraling stems
19 of the *juncus effusus* grass (**Fig. 4m**).



1
2 **Figure 4.** Shape- and location-specific 2D-3D transformation. a) *Albuca namaquensis* grass. b-d) Microcoils
3 with different pitches and diameters achieved by varying DoC along the thickness direction. e) Lotus flower. f-
4 i) Microflowers at different blooming stages achieved by varying DoC along both the thickness and radial
5 directions. j-l) Targeted transformations at one, two, and four petals. m) *Juncus effusus spiralis* grass. n-q)
6 Microhelices with different spins achieved by manipulating the 3D gradient of DoC periodically.

7
8 *Advantages of 2D-3D transformation over direct 3D printing*

9 Additionally, 2D-3D transformation can fabricate complicated and delicate 3D objects which
10 easily collapse, are flawed, or require special protocols in direct 3D printing [37]. **Figure 5**
11 shows that the 2D-3D transformation achieves microcoils with obviously smoother surfaces and
12 improved integrity, while the directly printed 3D structures show obvious stepping features. The
13 intrinsic layer-by-layer manner in direct 3D printing leads to inevitable stepping features on
14 curved surfaces. The unpredictable instability of over-hanging features during direct 3D printing
15 causes failure in fabrication, imperfect stitching of adjacent parts, and more surface roughness
16 (**Fig. S16**). Both intrinsic limitations in direct 3D printing are circumvented using the 2D-3D
17 transformation. Furthermore, the 2D-3D transformation fabricates complex objects in shorter
18 times, e.g., microcoils and microstents are fabricated three to four times faster than direct 3D
19 printing (**Fig. S17**).



1
2 **Figure 5.** Advantages of the 2D-3D transformation approach over direct 3D printing. a, b) and d, e) SEM
3 images of the same microcoil structure fabricated through direct 3D printing and 2D-3D transformation,
4 respectively. b) and e) are the magnified images of a) and d), respectively. c) and f) are profiling results at the
5 surface areas marked by red dashed lines in b) and e), respectively.

6
7 All results above were achieved using the IP-Dip resin. Also, we have tested implementing our
8 approach with other photoresists, including the IP-S resin and, more generally, the SU-8 resin.
9 Both resins have higher Young's modules than the IP-Dip resin, making the structural
10 transformations more difficult. Nevertheless, we succeeded in using both resins to fabricate the
11 entire standing flowers (**Fig. S18**), verifying the material independency of our approach. Besides,
12 we believe that the concepts demonstrated in this study can be important for addressing general
13 challenges (e.g., deformation) in the fabrication of 3D micro/nanoscale structures designed for
14 different devices and functions [38]. One representative example is the fabrication of 3D curved
15 lattice structures which are major components of architected metamaterials and micromachines
16 [39, 40]. Usually, such 3D lattice structures can only be fabricated via 3D printing. We further
17 demonstrated the capability to flexibly control their curved orientations and spatial topologies

1 which are challenging in direct 3D printing (**Fig. S19**). By setting appropriate DoC gradients
2 during printing, the lattice structure transformed to a bridge-shaped geometry with all lattice
3 features well maintained. The capability to control the spatial orientations and topologies of the
4 3D lattice structures can inspire new insights and designs of novel architected metamaterials
5 and micromachines for various functionalities. In addition, when combined with advanced beam
6 focusing and scanning systems, such as micro-lens arrays, spatial light modulators, and other
7 multi-foci techniques, the throughput of this approach can be significantly improved to meet the
8 needs in practical applications [41].

9 10 **Conclusions**

11 In this research, we present a general, controllable, and flexible strategy for 2D-3D structural
12 transformation at the microscale, which lays a foundation for constructing diverse, complex 3D
13 objects from 2D patterns. We succeeded in establishing spatially distributed stresses by tailoring
14 the spatial gradients of cross-links in photocurable polymers via TPP. The relationships among
15 the polymerization conditions, polymer shrinkages, and internal stresses were investigated.
16 Multi-mode 2D-3D transformations, including bending, rolling, coiling, waving, spiraling, and
17 out-of-plane distortions, were realized either individually or simultaneously in a single process.
18 Various 3D geometries, such as micro coils, waves, caps, flowers, helices, and micro-origamis,
19 were demonstrated with their transformation states and geometries being controlled precisely,
20 mimicking unique morphologies and different growing stages of natural plants. Such a 2D-3D
21 transformation approach also circumvents the intrinsic limitations of stepping and stitching in
22 direct 3D printing via TPP, achieving 3D objects with much smoother surfaces and improved
23 integrity.

24 25 **Materials and methods**

26 *Two-photon lithography of 2D layered patterns:* Two-dimensional polymer layered patterns
27 were fabricated using a commercial TPP system (Photonic Professional GT from Nanoscribe
28 GmbH) with three commercial photoresists: the IP-Dip and IP-S resins from Nanoscribe GmbH,
29 and the SU-8 resin (SU-8 2005) from MicroChem. The dip-in laser lithography (DiLL)
30 configuration was used for printing with the IP-Dip resin, while the oil immersion configuration
31 was used for printing with both the IP-S and SU-8 resins. The fs laser was focused by a Carl
32 Zeiss Plan-Apochromat objective lens (63× NA1.4 Oil DIC M27) and scanned by a computer-
33 controlled galvo in the resins to prepare arbitrary 2D layered patterns with designed DoC
34 gradients. The specific printing conditions for bulk shrinkage tests with the IP-Dip resin are
35 summarized in the **Supplemental Table**. For the SU-8 resin, prebaking (sequentially at 50 °C for
36 5 min, 65 °C for 30 min, and 95 °C for 75 min) was applied, followed by cooling down naturally
37 to room temperature before TPP printing.

38 *Sample development:* Both entire standing-flower structures printed with the IP-Dip and IP-S
39 resins were immersed in propylene glycol monomethyl ether acetate (PGMEA) (3M Company)
40 for 1 h to thoroughly dissolve the unreacted resin after the TPP printing, followed by a rinse in 2-
41 propanol (Sigma-Aldrich) for 20 min. The entire standing flower printed with the SU-8 resin was
42 rinsed in PGMEA for 12 h and then in acetone (Sigma-Aldrich) for 20 min. To prevent the
43 collapse of their structures due to capillary forces, the standing-flowers were subsequently dried
44 using a critical-point dryer (Tousimis Autosamdri 931) with slow-fill pressure, fill time, purge
45 time, post purge time, critical point time, and vent pressure set at 700 PSI, 150 s, 10 min, 90 s,

1 120 s, and 550 PSI, respectively [42]. The other structures printed with the IP-Dip resin were
2 also immersed in PGMEA for 1 h at first before immersed in NOVEC-7100 engineering fluidics
3 (3M Company) for 10 min and left to dry naturally under the ambient condition.

4 *Sample characterization and shrinkage measurement:* A Hitachi S4700 field-emission scanning
5 electron microscope (FE-SEM) was used to observe the shapes and morphologies of the 3D
6 structures after the transformation. The dark-field and green-fluorescence images in **Fig. 1** were
7 collected using an Olympus AX70 microscope with either a 20× or 40× objective lens. The
8 excitation wavelength of ~550-570 nm and the emission of fluorescent light in a wavelength
9 range of ~580-600 nm were used for fluorescence imaging [43]. The dimensions of the printed
10 samples were measured by ImageJ software on their SEM images, through which their volume
11 and directional shrinkages were calculated.

12 *Doc measurement:* Raman spectroscopy was used to determine the DoC of the TPP reaction.
13 Raman spectra were acquired by a Renishaw inVia H 18415 Raman microscope. The excitation
14 source was an argon laser with a wavelength of 785 nm and a power of 50 mW. The excitation
15 and signal collections were carried out using a 50× objective lens with a numerical aperture of
16 0.50. Raman spectra were recorded using an accumulation time of 15 s. The DoC values were
17 calculated from the Raman peak intensities of C=C and C=O as:

$$18 \quad \text{DoC} = 1 - \left(\frac{A_{C=C}/A_{C=O}}{A'_{C=C}/A'_{C=O}} \right), \quad (3)$$

19 where $A_{C=C}$, $A_{C=O}$ and $A'_{C=C}$, $A'_{C=O}$ are the integrated intensities of the corresponding peaks in the
20 TPP structures and the unpolymerized resin, respectively. Besides, a Nikon A1R confocal
21 fluorescence microscope was used for mapping DoC under different laser doses using the Nikon
22 NIS-Elements imaging acquisition and analysis program.

23 *Profile measurement:* The structural profiles were measured by a Keyence laser scanning
24 microscope (VK-X200K) which works at a laser wavelength of 408 nm. A Nikon objective lens
25 (CF Plan Apo, 150×, NA 0.95) was used to capture the fine details on the structure surfaces.

26 **Supplementary data**

27 Supplementary data to this article can be found online.

28 **Conflict of Interest**

29 The authors declare no conflict of interest.

30 **Acknowledgements**

31 Aofei Mao and Peixun Fan contributed equally to this work. The research was partially
32 supported by the National Science Foundation (under Award CMMI 1826392) and Nebraska
33 Center for Energy Sciences Research (NCESR). The research was performed in part in the
34 Nebraska Nanoscale Facility: National Nanotechnology Coordinated Infrastructure and the
35 Nebraska Center for Materials and Nanoscience (and/or NERCF), which are supported by the
36 National Science Foundation under Award ECCS: 2025298, and the Nebraska Research
37 Initiative.

1 **Data Availability**

2 The raw/processed data required to reproduce these findings cannot be shared at this time due to
3 technical or time limitations. However, most materials and processing parameters and conditions
4 are provided in the Supplementary Materials.

6 **References**

- 7 [1] Q. Liu, W. Wang, M.F. Reynolds, M.C. Cao, M.Z. Miskin, T.A. Arias, D.A. Muller, P.L.
8 McEuen, I. Cohen, *Sci. Robot.* 6 (2021) eabe6663.
- 9 [2] D. Rus, M.T. Tolley, *Nat. Rev. Mater.* 3 (2018) 101–112.
- 10 [3] M. del Pozo, C. Delaney, C.W.M. Bastiaansen, D. Diamond, A.P.H.J. Schenning, L.
11 Florea, *ACS Nano* 14 (2020) 9832–9839.
- 12 [4] M. Wang, B.-P. Lin, H. Yang, *Nat. Commun.* 7 (2016) 13981.
- 13 [5] S. Miao, N. Castro, M. Nowicki, L. Xia, H. Cui, X. Zhou, W. Zhu, S. Lee, K. Sarkar, G.
14 Vozzi, Y. Tabata, J. Fisher, L.G. Zhang, *Mater. Today* 20 (2017) 577–591.
- 15 [6] R. Fernandes, D.H. Gracias, *Adv. Drug Deliv. Rev.* 64 (2012) 1579–1589.
- 16 [7] C. Cui, D.-O. Kim, M.Y. Pack, B. Han, L. Han, Y. Sun, L.-H. Han, *Biofabrication* 12
17 (2020) 045018.
- 18 [8] Y. Zhou, A.W. Hauser, N.P. Bende, M.G. Kuzyk, R.C. Hayward, *Adv. Funct. Mater.* 26
19 (2016) 5447–5452.
- 20 [9] Y.-L. Zhang, Y. Tian, H. Wang, Z.-C. Ma, D.-D. Han, L.-G. Niu, Q.-D. Chen, H.-B. Sun,
21 *ACS Nano* 13 (2019) 4041–4048.
- 22 [10] L. Dong, A.K. Agarwal, D.J. Beebe, H. Jiang, *Nature* 442 (2006) 551–554.
- 23 [11] T. Xie, *Nature* 464 (2010) 267–270.
- 24 [12] Y.-Y. Gao, Y.-L. Zhang, B. Han, L. Zhu, B. Dong, H.-B. Sun, *ACS Appl. Mater.*
25 *Interfaces* 11 (2019) 37130–37138.
- 26 [13] Y.-F. Zhang, N. Zhang, H. Hingorani, N. Ding, D. Wang, C. Yuan, B. Zhang, G. Gu, Q.
27 Ge, *Adv. Funct. Mater.* 29 (2019) 1806698.
- 28 [14] L. Hines, K. Petersen, G.Z. Lum, M. Sitti, *Adv. Mater.* 29 (2017) 1603483.
- 29 [15] Y. Kim, H. Yuk, R. Zhao, S.A. Chester, X. Zhao, *Nature* 558 (2018) 274–279.
- 30 [16] N. Bassik, G.M. Stern, D.H. Gracias, *Appl. Phys. Lett.* 95 (2009).
- 31 [17] C. Py, P. Reverdy, L. Doppler, J. Bico, B. Roman, C.N. Baroud, *Phys. Rev. Lett.* 98
32 (2007) 156103.
- 33 [18] T.G. Leong, P.A. Lester, T.L. Koh, E.K. Call, D.H. Gracias, *Langmuir* 23 (2007) 8747–
34 8751.
- 35 [19] Q. He, T. Okajima, H. Onoe, A. Subagyo, K. Sueoka, K. Kuribayashi-Shigetomi, *Sci.*
36 *Rep.* 8 (2018) 4556.
- 37 [20] S. Xu, Z. Yan, K.-I. Jang, W. Huang, H. Fu, J. Kim, Z. Wei, M. Flavin, J. McCracken, R.
38 Wang, A. Badea, Y. Liu, D. Xiao, G. Zhou, J. Lee, H.U. Chung, H. Cheng, W. Ren, A.
39 Banks, X. Li, U. Paik, R.G. Nuzzo, Y. Huang, Y. Zhang, J.A. Rogers, *Science* 347 (2015)
40 154–159.
- 41 [21] T. Watanabe, M. Akiyama, K. Totani, S.M. Kuebler, F. Stellacci, W. Wenseleers, K.
42 Braun, S.R. Marder, J.W. Perry, *Adv. Funct. Mater.* 12 (2002) 611–614.
- 43 [22] B. Han, Y.-L. Zhang, L. Zhu, Y. Li, Z.-C. Ma, Y.-Q. Liu, X.-L. Zhang, X.-W. Cao, Q.-D.
44 Chen, C.-W. Qiu, H.-B. Sun, *Adv. Mater.* 31 (2019) 1806386.
- 45 [23] D. Jin, Q. Chen, T.-Y. Huang, J. Huang, L. Zhang, H. Duan, *Mater. Today* 32 (2020) 19–
46 25.

- 1 [24] A. Nishiguchi, H. Zhang, S. Schweizerhof, M.F. Schulte, A. Mourran, M. Möller, ACS
2 Appl. Mater. Interfaces 12 (2020) 12176–12185.
- 3 [25] C.L. Lay, M.R. Lee, H.K. Lee, I.Y. Phang, X.Y. Ling, ACS Nano 9 (2015) 9708–9717.
- 4 [26] Q. Sun, K. Ueno, H. Misawa, Opt. Lett. 37 (2012) 710.
- 5 [27] A.A. Bauhofer, S. Krödel, J. Rys, O.R. Bilal, A. Constantinescu, C. Daraio, Adv. Mater.
6 29 (2017) 1703024.
- 7 [28] L.J. Jiang, Y.S. Zhou, W. Xiong, Y. Gao, X. Huang, L. Jiang, T. Baldacchini, J.-F.
8 Silvain, Y.F. Lu, Opt. Lett. 39 (2014) 3034.
- 9 [29] M. Jamal, A.M. Zarafshar, D.H. Gracias, Nat. Commun. 2 (2011) 527.
- 10 [30] T. Baldacchini, M. Zimmerley, C.-H. Kuo, E.O. Potma, R. Zadoyan, J. Phys. Chem. B
11 113 (2009) 12663–12668.
- 12 [31] J. Bauer, A.G. Izard, Y. Zhang, T. Baldacchini, L. Valdevit, Adv. Mater. Technol. 4
13 (2019) 1900146.
- 14 [32] C. Lv, X.-C. Sun, Y.-S. Xu, W.-Y. Zhang, P. Li, Q. Shi, L. Wang, G. Wang, X.-W. Cao,
15 S.-X. Li, Y.-Z. Dai, H. Xia, H.-B. Sun, IEEE Sens. J. 18 (2018) 8796–8802.
- 16 [33] A. Sydney Gladman, E.A. Matsumoto, R.G. Nuzzo, L. Mahadevan, J.A. Lewis, Nat.
17 Mater. 15 (2016) 413–418.
- 18 [34] Y. Tao, Y.-C. Lee, H. Liu, X. Zhang, J. Cui, C. Mondoa, M. Babaei, J. Santillan, G.
19 Wang, D. Luo, D. Liu, H. Yang, Y. Do, L. Sun, W. Wang, T. Zhang, L. Yao, Sci. Adv. 7
20 (2021) eabf4098.
- 21 [35] O.G. Schmidt, K. Eberl, Nature 410 (2001) 168–168.
- 22 [36] Y. Mei, G. Huang, A.A. Solovev, E.B. Ureña, I. Mönch, F. Ding, T. Reindl, R.K.Y. Fu,
23 P.K. Chu, O.G. Schmidt, Adv. Mater. 20 (2008) 4085–4090.
- 24 [37] A.J. Gross, K. Bertoldi, Small 15 (2019) 1902370.
- 25 [38] D. Karnaushenko, T. Kang, V. K. Bandari, F. Zhu, O. G. Schmidt, Adv. Mater. 32 (2020)
26 1902994.
- 27 [39] L.R. Meza, S. Das, J.R. Greer, Science (2014).
- 28 [40] T.A. Schaedler, A.J. Jacobsen, A. Torrents, A.E. Sorensen, J. Lian, J.R. Greer, L.
29 Valdevit, W.B. Carter, Science 334 (2011) 962–965.
- 30 [41] C. N. Saggau, F. Gabler, D. D. Karnaushenko, D. Karnaushenko, L. Ma, O. G. Schmidt,
31 Adv. Mater. 32 (2020) 2003252.
- 32 [42] A. Vyatskikh, S. Delalande, A. Kudo, X. Zhang, C.M. Portela, J.R. Greer, Nat. Commun.
33 9 (2018) 593.
- 34 [43] A. Accardo, M.C. Blatché, R. Courson, I. Loubinoux, C. Thibault, L. Malaquin, C. Vieu,
35 Small 13 (2017) 1700621.